12-22-2007

Tidal Asymmetry and Residual Circulation Over Linear Sandbanks and their Implication on Sediment Transport: A Process-Oriented Numerical Study

Rosario Sanay
University of South Carolina - Columbia

George Voulgaris
University of South Carolina - Columbia, gvoulgaris@geol.sc.edu

John C. Warner

Publication Info

Published in *Journal of Geophysical Research*, Volume 112, Issue C12015, 2007, pages 1-15.
Sanay, R., Voulgaris, G., & Warner, J. C. (2007). Tidal asymmetry and residual circulation over linear sandbanks and their implication on sediment transport: A process-oriented numerical study. *Journal of Geophysical Research, 112* (C12015), 1-15.

Tidal asymmetry and residual circulation over linear sandbanks and their implication on sediment transport: A process-oriented numerical study

Rosario Sanay,[1] George Voulgaris,[1] and John C. Warner[2]

Received 12 January 2007; revised 24 July 2007; accepted 17 September 2007; published 22 December 2007.

[1] A series of process-oriented numerical simulations is carried out in order to evaluate the relative role of locally generated residual flow and overtides on net sediment transport over linear sandbanks. The idealized bathymetry and forcing are similar to those present in the Norfolk Sandbanks, North Sea. The importance of bottom drag parameterization and bank orientation with respect to the ambient flow is examined in terms of residual flow and overtide generation, and subsequent sediment transport implications are discussed. The results show that although the magnitudes of residual flow and overtides are sensitive to bottom roughness parameterization and bank orientation, the magnitude of the generated residual flow is always larger than that of the locally generated overtides. Also, net sediment transport is always dominated by the nonlinear interaction of the residual flow and the semidiurnal tidal currents, although cross-bank sediment transport can occur even in the absence of a cross-shore residual flow. On the other hand, net sediment divergence/convergence increases as the bottom drag decreases and as bank orientation increases. The sediment erosion/deposition is not symmetric about the crest of the bank, suggesting that originally symmetric banks would have the tendency to become asymmetric.

Citation: Sanay, R., G. Voulgaris, and J. C. Warner (2007), Tidal asymmetry and residual circulation over linear sandbanks and their implication on sediment transport: A process-oriented numerical study, *J. Geophys. Res.*, *112*, C12015, doi:10.1029/2007JC004101.

1. Introduction

[2] Shoals with horizontal scales of kilometers and several meters in height can be found in ambient depths varying from a few to tens of meters. They are common features worldwide on sandy shelves, in both tidally [*Caston*, 1972; *Swift et al.*, 1978, *Williams et al.*, 2000] and storm dominated environments [*Duane et al.*, 1972; *Swift et al.*, 1978; *Swift and Field*, 1981; *Parker et al.*, 1982]. These shoals have a profound effect on the hydrodynamics of coastal regions and the processes that form and maintain these features remain a fundamental question in oceanography and morphodynamics. Practical applications include the effect of shoals on navigation and dredging operations, as well as their use as sand sources for various nourishment projects and capping of dredge spoil.

[3] Tidally dominated shoals, also known as linear sandbanks or tidal sand ridges, are rhythmic features with typical length and width scales of the order of 10 km (up to 80 km) and 1 km, respectively [*Dyer and Huntley*, 1999]; they are found in continental shelves with abundant sand supply and strong (over 0.5 m s^{-1}) tidal current. The height of the linear sand banks represents appreciable fraction of the mean water depth, while their spacing appears to be a function of the width of the individual banks. In the Northern Hemisphere, the main axis of these banks is orientated a few degrees ($0°–20°$) anticlockwise with respect to the principal direction of the tidal currents. The bank cross section is slightly asymmetric with their steep face reaching a maximum angle of 6° to the horizontal [*Collins et al.*, 1995]. Furthermore some sandbanks (i.e., Norfolk and Flemish sand bank systems, North Sea) coexist with megaripples/sand waves systems with height and wavelength scales of the order of 1 and 10 m, respectively [see *McCave*, 1971; *McCave and Langhorne*, 1982; *Collins et al.*, 1995; *Vanwesenbeeck and Lanckneus*, 2000, and references therein]. These smaller-scale bed forms have been used as indicators of net sediment transport direction [see *Vanwesenbeeck and Lanckneus*, 2000] but also their presence influences circulation patterns through the introduction of large roughness scale (i.e., form drag).

[4] A number of theoretical and observational studies have been carried out to elucidate the hydrodynamics and morphodynamics (i.e., growth and maintenance) associated with linear sandbanks. An extended review of these studies is given by *Pattiaratchi and Collins* [1987], *Dyer and Huntley* [1999], and *Blondeaux* [2001]. *Huthnance* [1973] was the first investigator to study the mean circulation over

[1]Marine Science Program, Department of Geological Sciences, University of South Carolina, Columbia, South Carolina, USA.
[2]U.S. Geological Survey, Woods Hole, Massachusetts, USA.

0148-0227/07/2007JC004101

linear sandbanks; he used a simplified version of the depth-averaged shallow water equations to describe the basic mechanisms of tidal rectification over variable bottom topography. Coriolis force and bottom drag were found to be the two mechanisms leading to the generation of mean circulation, which deflects toward the crest because of an increase of bottom friction with decreasing water depth. The cross-isobath (i.e., cross-bank) velocity component increases to satisfy continuity, while the along-isobath (i.e., along-bank) component decreases in response to increased bottom friction. *Zimmerman* [1980] used vorticity dynamics and described ''Coriolis'' (topographic vortex stretching) and ''depth gradient'' (differential velocity torque due to the gradient of the depth-dependent friction), as the two mechanisms that produce residual vorticity. These results were later extended by *Gross and Werner* [1993] to include the effect of spatial variation of bottom drag or ''roughness gradient'' mechanism as a source of residual vorticity. The resulting current pattern from all mechanisms described above is a residual flow around the bank with a direction (i.e., clockwise or anticlockwise) that depends on the orientation of the bank with respect to the main tidal flow. Also, for the roughness gradient mechanism, the direction of the residual flow will depend on the sign of the bottom roughness gradient. For example a roughness pattern rough-smooth-rough, the residual circulation expected is anticlockwise. Overall, all three mechanisms interact with each other and can enhance or compete with each other on the overall residual vorticity production.

[5] Initial studies on the process of formation of the linear sandbanks were based on linear stability analysis. *Huthnance* [1982a] was the first to propose that linear sandbanks may form as a result of instability of the system. Considering shallow water dynamics and a nonlinear relationship between the currents and sand transport, he suggested that tidal rectification due to the presence of the bank drives sediment transport toward the crest. The currents turn upslope, toward the crest, as they approach the bank and are stronger in magnitude than the downslope directed currents. This leads to a net sediment transport toward the crest and hence to bank growth. This model although it assumes straight, infinitive banks, it seems to explain much of the observed circulation features of sandbanks located far from the coast, including growth rate, bank orientation and wavelength. *Huthnance* [1982a] also analyzed the equilibrium cross-sectional profile of the bank and found that the asymmetrical shape is due to the action of the residual currents. *Huthnance* [1982b] extended his work for the case of finite banks, but without including the action of Coriolis or inertial terms. Later on, *Hulscher et al.* [1993] presented a model where the complete form of the shallow water equations was used to describe the dynamics under tidal forcing. *Besio et al.* [2006] proposed a fully three-dimensional weakly nonlinear model to study the generation of tidal sand waves and sanbanks from small bottom perturbations. Their model predicts that in the Northern Hemisphere the orientation of the sandbanks can be either clockwise or anticlockwise dependent on the sign of the rotation of the velocity vectors induced by the tides.

[6] Although the models resulting from stability analysis techniques explain much of the features of linear sandbanks, they are limited in that the height of the bed forms has to be small compared to the water depth, which is not a common case in nature. Furthermore, the finite amplitude evolution of the banks cannot be predicted using a linear approach as that employed in stability analyses. With these limitations in mind, *Roos et al.* [2004] presented a nonlinear morphodynamic model that includes surface wind wave action and allows the tidal flow to be asymmetric through the inclusion of higher harmonics and a residual flow. At this juncture it should be noted that those components were superimposed on a prescribed symmetrical tidal flow and as such were fully decoupled from the bank morphology and its interaction with the flow. They found that both wave stirring and the degree of asymmetry of the flow play an important role on controlling the height of the bank, while flow asymmetry also influences the degree of the asymmetry of the cross-sectional shape of the bank.

[7] In this paper, we explore the importance of the overtides (higher harmonics) and residual circulation (time average over one tidal cycle) on the sediment transport on linear sandbanks. Instead of prescribing the nonlinearities to the tidal forcing as was done by *Roos et al.* [2004], we use a fully nonlinear hydrodynamic numerical model (Regional Ocean Model System, ROMS) that allows their local generation through the interaction of the flow with bed morphology, roughness distribution and orientation of the linear banks. For the bottom drag parameterization, both uniform and spatially variable bottom drag conditions are investigated, where the latter is intended as a representation of the development of sand waves with different sizes over the flanks of the banks. Although no direct estimates of sediment fluxes are carried out, the hydrodynamic numerical results are used to evaluate a sediment transport proxy vector (see section 2.2) in accordance to the method described by *Van der Molen* [2000]. The numerical model setup is presented is section 2. A baseline case is established and numerical experiments for drag coefficient spatial variability, bank orientation, and bank cross-sectional shape, are carried out. The results are discussed in terms of tidal and residual flows in section 3 while a diagnostic analysis of the momentum balance is presented in section 4. The implication of the developed hydrodynamics on sediment transport, for each case, is discussed in section 5, while the final conclusions are presented in section 6.

2. Methodology

[8] A total of 6 numerical experiments were carried out to study the local generation of overtides and residual circulation over linear sandbanks and to assess their significance in sediment transport (see Table 1). Results from each experiment are compared to a baseline case (case 1) that assumes symmetric, sinusoidal in shape bank cross section with a constant uniform bottom roughness and its axis rotated 10° anticlockwise with respect to the main tidal flow. In order to examine the importance of bottom roughness parameterization two numerical experiments (cases 2 and 3) were carried out using the same bathymetry as in case 1 but with increased bottom drag. This was spatially uniform in case 2 and variable in case 3. The significance of bank orientation is examined in cases 4 and 5, which are

Table 1. Summary of Numerical Experiments (Cases) Carried Out[a]

Case	*a*	Bank Profile	*Cd*
1	10°	symmetric	0.0035
2	10°	symmetric	0.0075
3	10°	symmetric	0.0025–0.0075
4	5°	symmetric	0.0025–0.0075
5	20°	symmetric	0.0025–0.0075
6	5°	asymmetric	0.0025–0.0075

[a]Here *a* is the angle between the tidal forcing and the main axis of the sandbank, and *Cd* is the drag coefficient (one value denotes constant roughness over the domain while a range denotes variable roughness with depth).

similar to case 3 with the exception that the orientation of the bank has been altered to 5° and 20°, respectively. Finally, case 6 simulates a bank with an asymmetric cross-sectional shape similar to that found in banks in the North Sea [*Collins et al.*, 1995; *Voulgaris et al.*, 2001].

2.1. Hydrodynamic Model

[9] The Regional Ocean Model System (ROMS) [*Haidvogel et al.*, 2000], a three dimensional, time-dependent oceanographic model governed by the hydrostatic primitive equations was used in this work. The Generic Length Scale (GLS) approach [*Umlauf and Burchard*, 2003; *Warner et al.*, 2005] is used to parameterize vertical mixing. The numerical domain consisted of a basin 200 × 200 km and 40 m deep, with a coastline boundary on the west side and three open boundaries located on the north, south and east, respectively (Figure 1). A series of 3 linear sandbanks was placed in the center of the domain aligned almost parallel to the coast. All banks are identical: 40 km long, 5 km wide, 25 m height and are spaced 10 km (crest to crest) apart. A Cartesian orthogonal coordinate system is used, with the x axis selected to coincide with the southern open boundary with positive offshore, while the y axis laid along the lateral wall (west boundary) at $x = 0$ and pointed toward the north (Figure 1). The horizontal grid spacing is variable ranging from 250 to 2000 m for symmetric banks setups and from 150 to 2000 m for the asymmetric banks. The finest grid is located over the banks and the spacing increases linearly (toward the four boundaries) to the maximum value at approximately 30 km from the bank field thereafter the resolution remains constant. A total of 15 vertical levels were used with increased resolution near the local bottom and free surface.

[10] The numerical experiments included all the terms of the primitive equations and assumed homogenous fluid conditions. A third-order and upstream biased advection scheme was used, so no explicit horizontal viscosity was required [*Haidvogel et al.*, 2000]. Momentum boundary condition on the surface is zero stress (no wind). Parameterization of the bottom stress is based on a logarithmic velocity profile. Both uniform and variable values of the bottom roughness length were used (see Table 1). These values were consistent with observational data from the Norfolk Banks at the North Sea (see section 3).

[11] Free slip conditions were established for the closed boundary and no-gradient conditions were used at the eastern open boundary for all variables. The model was forced with a free surface semidiurnal (M_2, 12 h period) tidal oscillation at the northern boundary in the form of a Kelvin wave. The amplitude of the Kelvin wave was chosen such that the current amplitude at the vicinity of the banks was 0.6 m s^{-1}, a value close to that reported by *Collins et al.* [1995] for the North Sea during neap tides. In both north and south boundaries, radiation condition on free surface elevation and momentum variables were prescribed. All the numerical experiments started from rest as the initial condition.

2.2. Harmonic Analysis

[12] Simulations were carried out for a total of 6 tidal cycles. Results are presented for the last tidal cycle, after which a dynamic equilibrium was established. The instantaneous horizontal velocity components (u, v) are assumed to consist of a residual flow (u_0, v_0) and three tidal harmonic components with amplitudes u_n and v_n, where n = 2, 4, or 6, respectively:

$$u = u_0 + u_2\cos(\omega t - \phi_{2x}) + u_4\cos(2\omega t - \phi_{4x}) + u_6\cos(3\omega t - \phi_{6x}) \quad (1)$$

$$v = v_0 + v_2\cos(\omega t - \phi_{2y}) + v_4\cos(2\omega t - \phi_{4y}) + v_6\cos(3\omega t - \phi_{6y}) \quad (2)$$

where ω is the frequency of the M_2 tidal component, t is time, and ϕ denotes phase while the subscripts 2, 4, and 6 represent semidiurnal, quarter-diurnal, and sixth-diurnal components. The values of residual flow (time average over one tidal cycle) and the amplitude and phase of each tidal component were estimated through a least squares fit of equations (1) and (2) to the numerical results.

2.3. Proxy Sediment Transport Parameterization

[13] In order to evaluate the relative contribution of the tide-induced (with tidal stirring) residual flow and the overtides to net sediment transport and to identify areas of sediment transport convergence/divergence, a simple transport relationship (containing the essential transport properties) for tidally averaged sediment transport was defined following *Van der Molen* [2000]:

$$\vec{S} = \left\langle |U|^2 \cdot \vec{U} \right\rangle \quad (3)$$

where $\vec{U}$ is the Cartesian velocity vector near the bed, where the majority of the sediment transport take place, and the brackets denote tidally averaged quantities. At this juncture we should note that equation (3) does not include a threshold (critical) condition for initiation of sediment. Omission of the critical condition is implemented for simplification purposes and it has been applied to previous work [see, e.g., *Dronkers*, 2005, p. 151; *Trowbridge*, 1995] that relates with morphodynamical evolution. Further such an omission although alters the absolute magnitude of the sediment transport index it does not alter the spatial gradients presented in this study. By substituting

equations (1) and (2) into equation (3) and integrating over one tidal cycle, the x and y components (S_x and S_y, respectively) of the sediment transport parameter can be written as:

$$\begin{aligned} S_x = & \left\{ u_0 \left[\left(u_0^2 + v_0^2\right) + \frac{1}{2}\left(3u_2^2 + v_2^2\right) + \frac{1}{2}\left(3u_4^2 + v_4^2\right) + \frac{1}{2}\left(3u_6^2 + v_6^2\right) \right] \right. \\ & \left. + v_0 \left[-u_2 v_2 \cos\left(\varphi_{2x} - \varphi_{2y}\right) + u_4 v_4 \cos(\varphi_{4x} - \varphi_{4x}) + u_6 v_6 \cos\left(\varphi_{6x} - \varphi_{6y}\right) \right] \right\} \qquad (I) \\ & + \left\{ u_4 \left[\frac{3}{4} u_2^2 \cos(-\varphi_{4x} + 2\varphi_{2x}) + \frac{1}{4} v_2^2 \cos\left(\varphi_{4x} - 2\varphi_{2y}\right) \right] \right. \\ & + \left[\frac{3}{2} u_2 u_4 u_6 \cos(-\varphi_{6x} + \varphi_{2x} + \varphi_{4x}) + \frac{1}{2} u_2 v_2 v_4 \cos\left(-\varphi_{4y} + \varphi_{2x} + \varphi_{2y}\right) \right. \\ & + \frac{1}{2} u_2 v_4 v_6 \cos\left(-\varphi_{6y} + \varphi_{2x} + \varphi_{4y}\right) + \frac{1}{2} u_4 v_2 v_6 \cos\left(-\varphi_{6y} + \varphi_{4x} + \varphi_{2y}\right) \\ & \left. \left. + \frac{1}{2} u_6 v_2 v_4 \cos\left(-\varphi_{4y} + \varphi_{6x} - \varphi_{2y}\right) \right] \right\} \qquad (II) \end{aligned} \tag{4}$$

and,

$$\begin{aligned} S_y = & \left\{ v_0 \left[\left(v_0^2 + u_0^2\right) + \frac{1}{2}\left(3v_2^2 + u_2^2\right) + \frac{1}{2}\left(3v_4^2 + u_4^2\right) + \frac{1}{2}\left(3v_6^2 + u_6^2\right) \right] \right. \\ & \left. + u_0 \left[-u_2 v_2 \cos\left(\varphi_{2x} - \varphi_{2y}\right) + u_4 v_4 \cos\left(\varphi_{4x} - \varphi_{4y}\right) + u_6 v_6 \cos\left(\varphi_{6x} - \varphi_{6y}\right) \right] \right\} \qquad (I) \\ & + \left\{ v_4 \left[\frac{3}{4} v_2^2 \cos\left(-\varphi_{4y} + 2\varphi_{2y}\right) + u_2^2 \cos\left(\varphi_{4x} - 2\varphi_{2y}\right) \right] \right. \\ & + \left[\frac{3}{2} v_2 v_4 v_6 \cos\left(-\varphi_{6y} + \varphi_{2y} + \varphi_{4y}\right) + \frac{1}{2} v_2 u_2 u_4 \cos\left(-\varphi_{4x} + \varphi_{2x} + \varphi_{2y}\right) \right. \\ & + \frac{1}{2} v_2 u_4 u_6 \cos\left(-\varphi_{6x} + \varphi_{2y} + \varphi_{4x}\right) + \frac{1}{2} v_4 u_2 u_6 \cos\left(-\varphi_{6x} + \varphi_{2x} + \varphi_{4y}\right) \\ & \left. \left. + \frac{1}{2} v_6 u_2 u_4 \cos\left(-\varphi_{6y} + \varphi_{2x} - \varphi_{4x}\right) \right] \right\} \qquad (II) \end{aligned} \tag{5}$$

[14] All terms in equations (4) and (5) are grouped within braces into two groups. Group I (hereafter referred to as $\boldsymbol{S}_{res}$) consists of the product of a sediment stirring parameter (factors inside the square brackets, units of $m^2\ s^{-2}$) that is responsible for making the sediment available for transport, and a sediment carrier parameter (factors outside the square brackets, units of $m\ s^{-1}$), such that it represents sediment transport due to residual flow. Group II (hereafter referred to as $\boldsymbol{S}_{asym}$) represents the contribution of tidal asymmetries to the total sediment transport ($\boldsymbol{S} = \boldsymbol{S}_{res} + \boldsymbol{S}_{asym}$). It should be noted that group II can be further separated into sediment stirring due to semidiurnal tidal component (factors inside the first set of brackets) and sediment transport due to quarter-diurnal component (i.e., M_4 contributes directly to sediment transport by being the carrier). All the remainder terms in group II consist of a combination among the different tidal constituents, so that the stirring and transport is due to the interaction of all tidal constituents.

[15] The relative contribution of $\boldsymbol{S}_{res}$ (i.e., term I) and $\boldsymbol{S}_{asym}$ (i.e., terms II) to the tidally averaged transport vector can be assessed using a dominance index (IDX), defined as [*Van der Molen*, 2000]:

$$IDX = \frac{|S_{res}| - |S_{asym}|}{|S_{res}| + |S_{asym}|} \tag{6}$$

so, that for $0 < IDX < 1$ net sediment transport is dominated by the residual flow, while for $-1 < IDX < 0$ tidal asymmetry dominates the net sediment transport.

3. Model Results on Tidal and Residual Circulation

[16] This section presents the results of the numerical simulation with respect to tidal and residual circulation for the various cases listed in Table 1. In order to minimize the influence from the end of the banks, model outputs are shown along a bank section (AA′ or BB′) located in the middle of the bank (see Figure 1). In the following, u and v are the across- and along-shelf velocity components, while u' and v' are the components in a rotated reference frame that coincides with the across- (x') and along-bank (y') axes, respectively (see Figure 1). The latter coordinate system is used to describe the development of the overtides and residual flows in relation to the bank morphology, while the former coordinate system in used to describe changes that are related with the effect of the banks on the propagation characteristics of the Kelvin wave. All vertical section plots portray views toward the north (i.e., toward the forcing open boundary). First the results for the baseline case (case 1) are described while differences for the other cases are presented subsequently.

3.1. Case 1 (Baseline)

3.1.1. Tidal Circulation

[17] Vertically integrated velocity fields are shown in Figure 2a in terms of the principal tidal constituent (M_2).

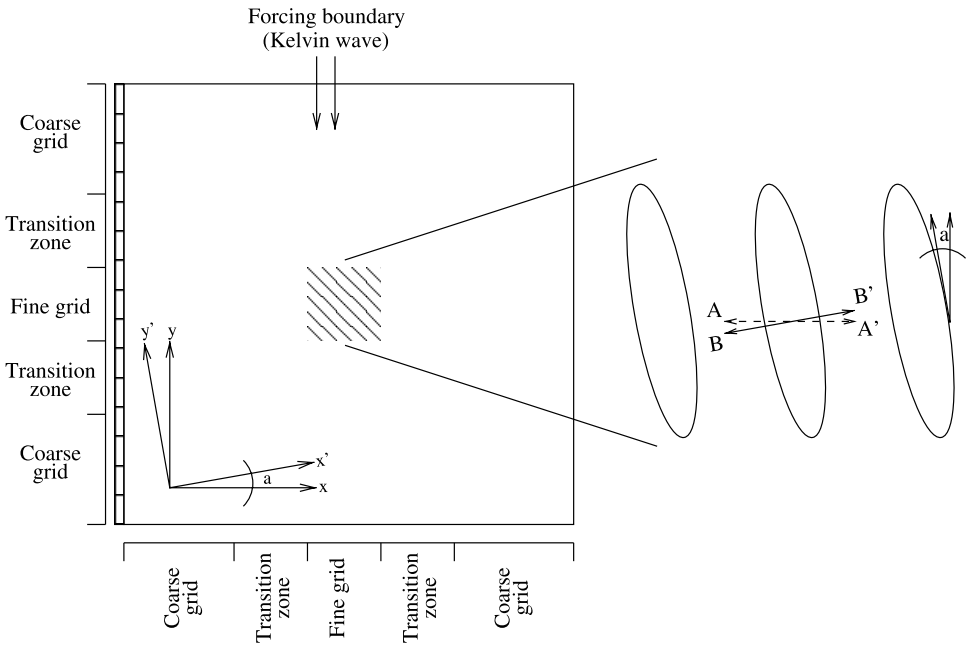

Figure 1. Schematic representation of the numerical model domain. The *x*-*y* coordinate system is aligned in the across- and along-shelf direction. The x'-y' coordinate system is aligned in the across- and along-bank direction. The cross-section plots shown in the manuscript are plotted along transect AA' (dashed line in middle bank) or transect BB' (solid line in the middle bank) with a view toward the North.

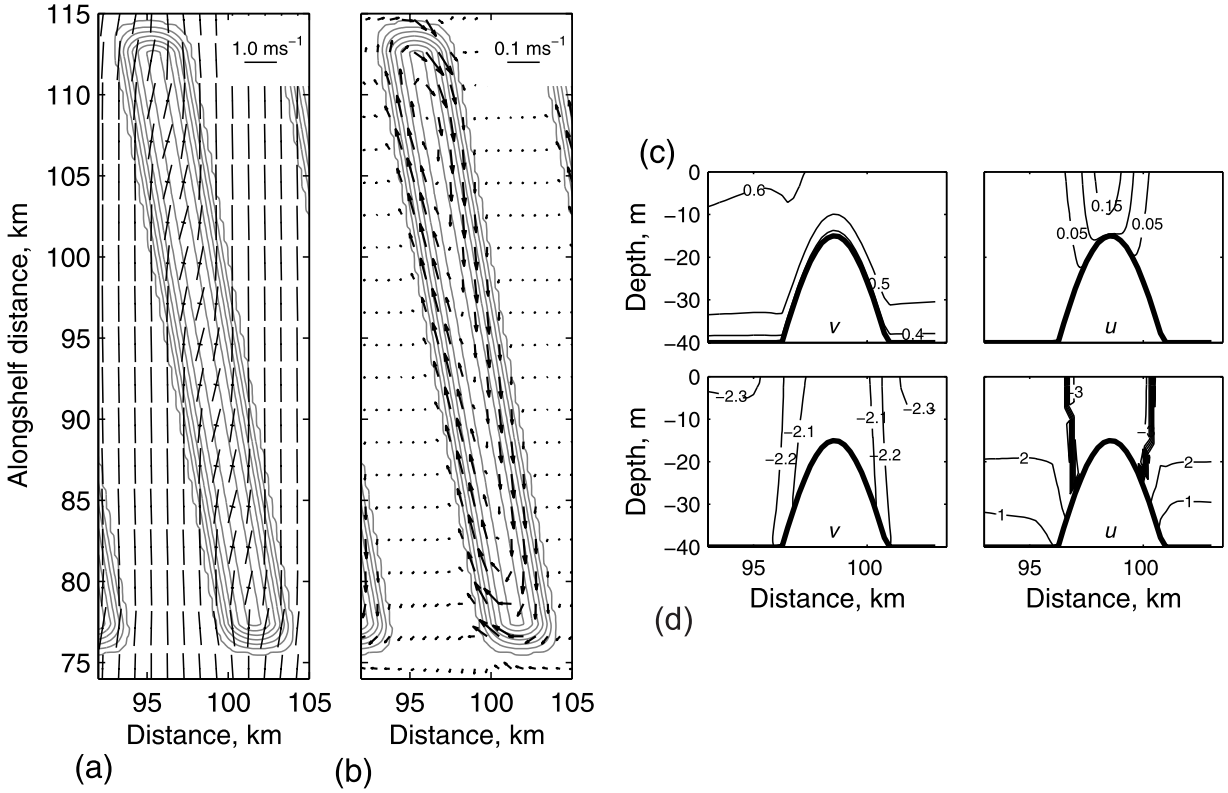

Figure 2. Model results corresponding to the baseline case. (a) M_2 vertically integrated tidal ellipses axes, (b) vertically integrated residual circulation, and (c) amplitude in m/s and (d) phase contours in radians of the along- and across-shelf semidiurnal tidal velocity components (along transect AA').

The major axes of the M_2 tidal ellipses are larger in the flat areas between the banks (swales) and decrease toward the crest of the bank. The bank crest is also the location where the minor axes get their maximum values. The minor axis decreases rapidly toward the swales, such that the M_2 tidal ellipses become rectilinear in between banks and aligned with the ambient flow (i.e., undisturbed flow away from the bank area). Over the bank, the major axis of the ellipses is tilted clockwise toward the crest as water depth decreases. The refraction of the major axes is consistent with theoretical models and observational data [*Voulgaris et al.*, 2002; *Griffiths et al.*, 2002; *Collins et al.*, 1995] and provides confidence on the model performance to this forcing.

[18] The M_2 tidal ellipse characteristics (orientation and magnitude of minor and major axes) described in the previous paragraph are uniform along the bank except near the ends of the bank, where the flow tends to be diverted around the ends rather than flowing directly over them. For this specific case, the horizontal scale of the influence of the ends of the bank is estimated to be approximately 1.5 times the width of the bank.

[19] The modulation of the tidal forcing due to the presence of the banks is better illustrated in the vertical distribution of the amplitude and phase of the along- and across-shelf velocity components along transect AA′ (Figures 2c and 2d). Away from the banks (not shown here), the distribution of the M_2 tidal current amplitude and phase of the along- and across-shelf velocity components describe a Kelvin wave. In contrast, over the bank, the lines of M_2 equal phase intersect the free surface, showing an across-shelf phase variation. Also, over the bank, the across-shelf velocity component becomes noticeable with maximum speed at the crest.

[20] Hereafter, tidal current characteristics described in the along-/across-bank reference frame, that are the directions of interest in this work (i.e., considering that the amplitudes control the sediment transport). The amplitudes of the M_4 and M_6 tidal currents and the magnitude of the residual flow outside the bank region is approximately 2–3 orders of magnitude smaller than the amplitude of the tidal forcing; they increase over the banks reaching values up to 10% of the magnitude of the M_2 currents.

[21] Vertical cross sections of the tidal characteristics (amplitude and phase) of the M_2, M_4 and M_6 constituents, corresponding to u' and v' velocity components along the transect BB′, are shown in Figures 3 and 4. The amplitude of the along-bank semidiurnal velocity component (v') follows the bathymetry and decreases toward the crest and toward the bottom because of the bottom friction effects (Figure 3). On the other hand, the across-bank semidiurnal velocity component (u' contours) shows a maximum near the sea surface at the crest of the bank because of mass conservation in response to the reduction of the total water depth. Notice that both horizontal velocity components (u', v') tend to be symmetric around the crest of the bank, but their cross-bank distribution is different.

[22] The amplitude of the along-bank M_4 velocity component shows two maxima located at the slopes of the bank suggesting that not only friction, but also advection terms might be important for the generation of the M_4 harmonic in this case (for detailed analysis see section 4). It is noticeable that the strongest quarter-diurnal currents occur at the eastern slope. The cross-bank M_4 velocity component obtains its maximum value over the bank crest diminishing to almost zero at the swales confirming that this harmonic is mainly the result of tidal rectification due to bathymetric changes. On the other hand, both the along- and across-bank M_6 velocity components exhibit maximum amplitudes near the bed at the crest of the bank, where frictional effects are maximum.

[23] The vertical distribution of the phase, for each tidal harmonic of u' and v', is shown in Figure 4. In general, the lateral distribution of the M_2 and M_6 phases for both velocity components (u', v') have the tendency to be symmetric around the crest of the bank, with the lines of equal phase intersecting the free surface. While the distribution pattern of the M_4 phase shows a delay between the east and west slopes for the across- and along-bank components. The result of this delay is a tidal asymmetry with a flood dominance on the eastern slope and an ebb dominance on the western slope driving a net sediment transport around the bank. This is further analyzed in section 5.

3.1.2. Residual Flow

[24] The vertically integrated residual flow is shown on Figure 2b; it creates a cyclonic eddy around the bank in accordance with previous theoretical [e.g., *Huthnance*, 1973] and observational data [e.g., *Caston and Stride*, 1970; *Collins et al.*, 1995; *Voulgaris et al.*, 2002; *Griffiths et al.*, 2002] for an anticlockwise rotated (with respect to the main tidal forcing) elongated bank in the Northern Hemisphere. Maximum vertically integrated residual currents are found at the slopes of the banks while on the swales the flow is at least 2 orders of magnitude smaller. The vertical structure of the horizontal velocity components of the mean flow along transect BB′ is shown in Figure 5. For the along-bank residual current (v'), the numerical model predicts two surface-intensified jet-like residual circulation patterns where the jet's cores are located over the slopes of the bank. Thus the clockwise eddy around the bank (see Figure 2b) is present throughout the water column. The residual currents are more energetic than the principal overtides, with maximum speeds of 0.06 m s^{-1} and they are found on both sides of the bank. The cross-bank velocity component (u') is directed toward the coast throughout the vertical and horizontal domain; its magnitude decreases rapidly toward the bed, such that the u'/v' ratio tends to approach zero, leading to a near-bed residual flow that is mostly directed along bank.

3.2. Influence of Bottom Roughness on Overtide and Residual Flux Generation (Cases 2 and 3)

[25] Field observations have shown the presence of megaripples/sand waves systems on both slopes of some linear sandbanks, while the crest of the banks are characterized predominantly by a smooth bed surface [e.g., *Collins et al.*, 1995; also unpublished side scan sonar data, 1999] implying a spatially variable drag coefficient due to form drag. Mean and maximum drag coefficient values of 3.5×10^{-3} and 7.5×10^{-3} have been reported for the Middelkerke Bank in the North Sea [*O'Connor*, 1996], while *Voulgaris et al.* [2002] have reported drag coefficient estimates on the Broken bank of 2.7×10^{-3}. In order to examine the effects of bottom roughness on overtide and

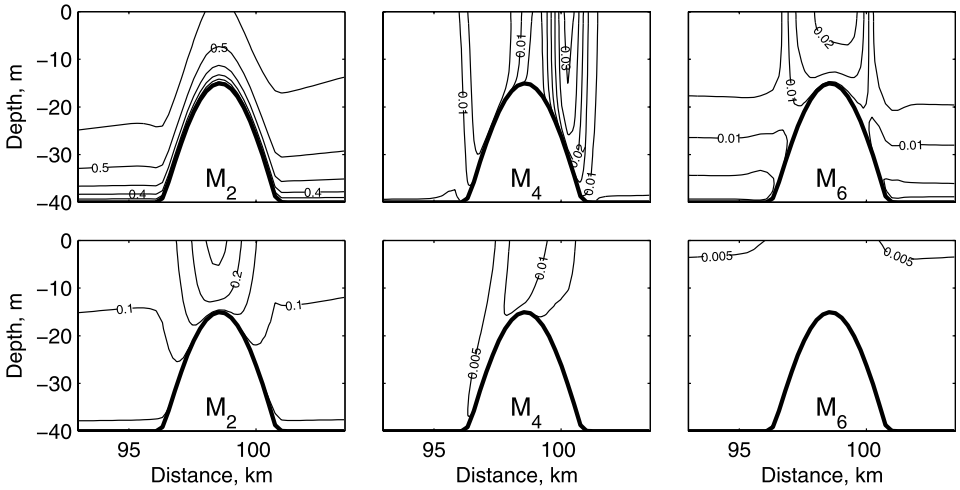

Figure 3. Amplitude of the (top) along- and (bottom) across-bank velocity components (v', u') for the three major tidal constituents corresponding to the baseline case, along transect BB'. Contours are in m/s.

residual flow generation, the bottom roughness was increased from 3.5×10^{-3} (case 1) to 7.5×10^{-3} (case 2) and spatially variable drag coefficient was used in case 3.

[26] The spatially variable bottom roughness is implemented where *Cd* varies linearly as a function of the total water depth. This approach was based on side scan sonar observations collected over the Broken Bank in 1999 [*Voulgaris et al.*, 2002] that demonstrate larger bed forms near the swales and plain bed at the crest. This bed form distribution leads to drag coefficients at the slopes of 7.5×10^{-3}, which is 3–4 times larger than that at the crest (mainly skin friction), which was found to be 2.7×10^{-3} [*Voulgaris et al.*, 2002].

[27] Figure 6 shows the vertical distribution of the magnitude ratio of the residual flow (V_{M_0}) and the overtides (V_{M_4}, V_{M_6}) to the speed of the semidiurnal tidal component (V_{M_2}, corresponding to each case at each location) along transect BB′ for cases 1, 2 and 3, (where $V = [u^2 + v^2]^{1/2}$). The results from these three cases indicate some common features: 1) the mean flow is more energetic than either of the overtides; 2) the mean flow is about 10% of the speed of the semidiurnal tidal component; 3) the ratios V_{M_4}/V_{M_2} and V_{M_6}/V_{M_2} are of the same order of magnitude; and 4) the cross-bank velocity component is at most 10% of the along-bank velocity component (not shown here). By increasing the drag coefficient from 3.5×10^{-3} to 7.5×10^{-3} (e.g., cases 1 and 2) all ratios increase, in response to the increased bottom friction effects. By using a spatial gradient in the bottom roughness (see case 3), the ratio V_{M_0}/V_{M_2} is reduced to a minimum value when compared to cases 1 and 2. This slight decrease in the mean flow is due to the "roughness gradient mechanism" that creates an anticlockwise residual vorticity for the bottom roughness pattern "rough-smooth-rough" [*Gross and Werner*, 1993], that competes with the clockwise residual vorticity induced by the "Coriolis mechanism" and the "depth gradient mech-

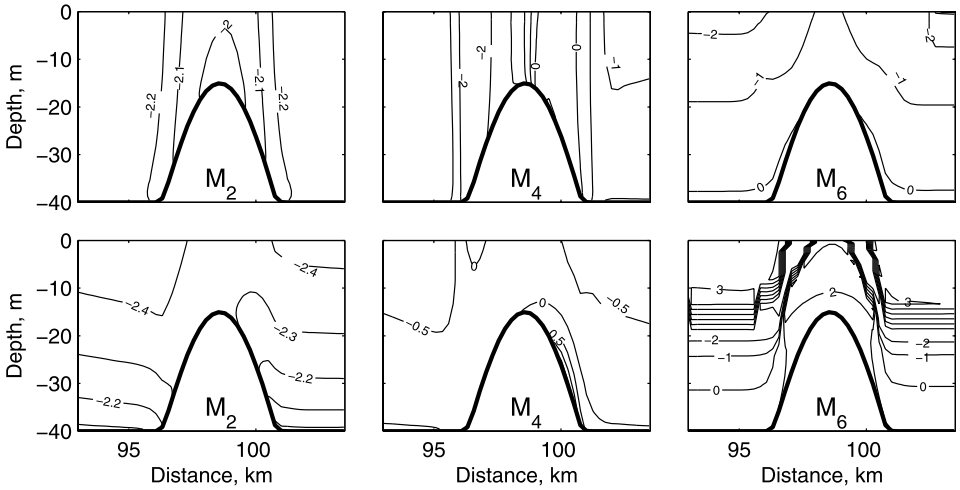

Figure 4. Phase of the (top) along- and (bottom) across-bank velocity component (v', u') for the three major tidal constituents corresponding to the baseline case, along transect BB'. Contours are in radians.

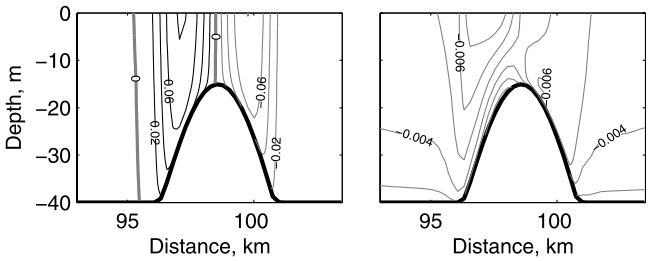

Figure 5. Residual flow of the (left) along- and (right) across-bank velocity component corresponding to the baseline case, along transect BB'. Velocity magnitude is in m/s. Black contours represent positive values, while gray contours represent negative values. The thick gray contour represents the zero isotach.

anism", for sandbanks rotated anticlockwise respect to the main tidal current.

3.3. Influence of Bank Orientation on Overtide and Residual Flux Generation

[28] The numerical experiments 3, 4 and 5 were carried out using spatially variable drag coefficients, symmetric cross-sectional bank profile and differ only on the bank orientation (10°,5°, and 20°, respectively; see Table 1). The vertical variability of the amplitude ratios V_{M_0}/V_{M_2}, V_{M_4}/V_{M_2}, V_{M_6}/V_{M_2} for these cases along transect BB′ is shown in Figure 7. The energy cascade toward the principal overtide (V_{M_4}) and residual flow (V_{M_0}) is intensified as the angle between the forcing tidal current and the main axis of the bank increases. The increased values of V_{M_4}/V_{M_2} correspond to the increased role of the advection terms (this is further analyzed in section 4). The residual flow increases because of increased differential velocity torque and torque due to gradient in depth-distributed friction, as described by *Zimmerman* [1980] and *Robinson* [1983]. This leads to an increase on residual vorticity and, in turn, on residual flux.

3.4. Influence of Bank Cross-Sectional Shape on Overtide and Residual Flux Generation

[29] The bathymetric profile in case 4 is a symmetric, sinusoidal in shape while that of case 6 corresponds to that of the Broken Bank in the North Sea [*Voulgaris et al.*, 2001, 2002]. The banks on both experiments are 25 m tall and 5 km wide. The slopes of the symmetric bank are approximately 0.6°. The slopes of the asymmetric bank are approximately 1° and 0.4°, respectively. Bank orientation, initial and forcing conditions and the bottom roughness parameterization (as a function of the total water depth) are identical for both cases.

[30] The locally generated overtides show similar magnitude and distribution pattern in both experiments (see cross-sectional plots of the ratio V_{M_4}/V_{M_2}, V_{M_6}/V_{M_2}in Figure 8), with the V_{M_4}/V_{M_2}ratio being larger on the eastern slope of the bank. The only remarkable difference is noted on the pattern of residual flow circulation (see Figures 8 and 9). The along-bank mean velocity (v_0') component in the symmetric bank case is slightly stronger on the eastern slope and the zero speed contour is located at the crest of the bank (Figure 9a). For the asymmetric bank case, the along-bank residual flow at the eastern side (steepest slope) is approximately twice of that observed on the western slope (Figure 9c).

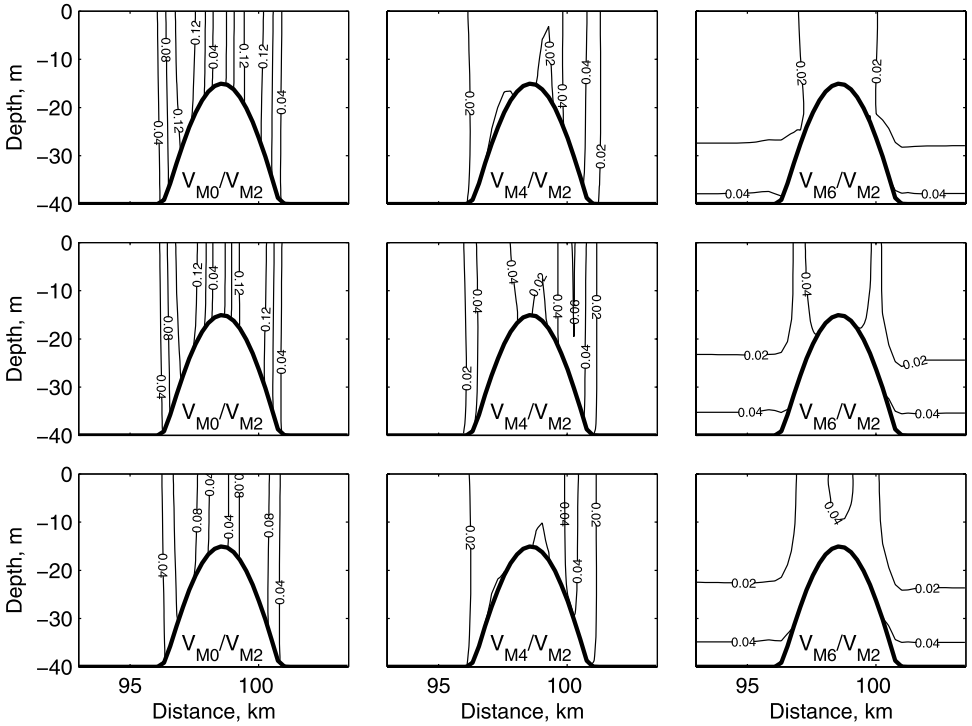

Figure 6. Effect of bottom roughness. Cross-section plots of the speed ratio of mean flow (V_{M0}) and each overtide (V_{M4}, V_{M6}) to the semidiurnal tidal component speed (V_{M2}), along transect BB′, corresponding to (top) case 1, (middle) case 2, and (bottom) case 3.

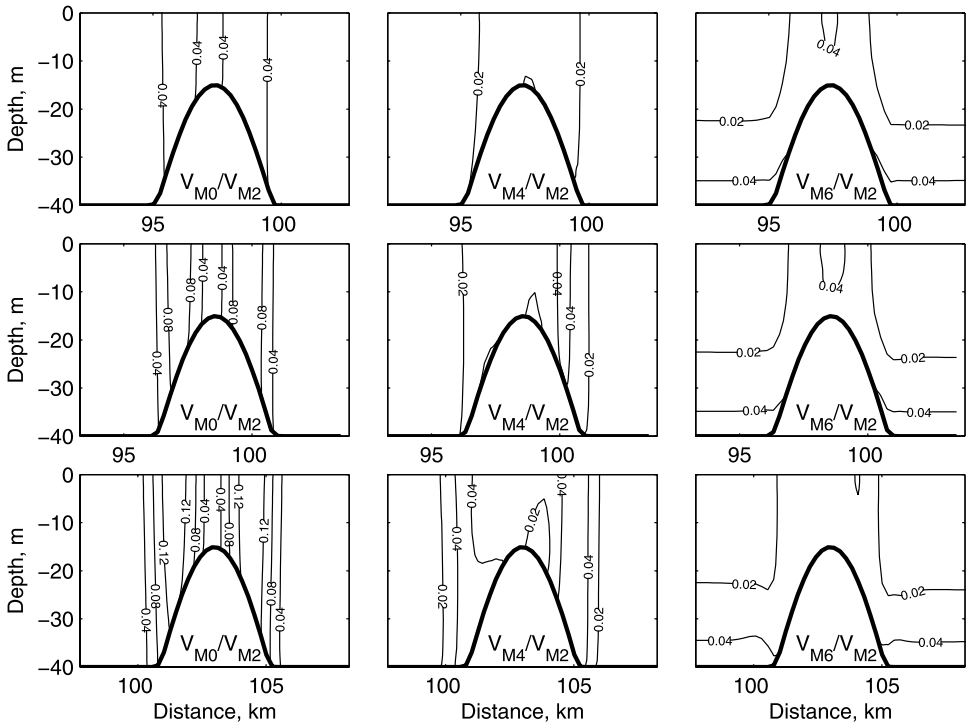

Figure 7. Effects of bank orientation. Cross-section plots of the speed ratio of mean flow (V_{M0}) and each overtide (V_{M4}, V_{M6}) to the semidiurnal tidal component speed (V_{M2}), along transect BB′, corresponding to (top) case 4 (5°), (middle) case 3 (10°), and (bottom) case 5 (20°).

The zero mean flow contour is offset to the western slope in agreement with residual flow measurements carried out over the Broken Bank using an autonomous underwater vehicle [*Griffiths et al.*, 2002; *Voulgaris et al.*, 2001]. The across-bank residual circulation over an asymmetric bank exhibits weak convergence toward the crest near the bed (Figure 9d), while the flow over a symmetric bank (Figure 9b) is similar to that found for the baseline case (case 1, i.e., directed toward the western boundary of the domain). Examination of the ratio V_{M_0}/V_{M_2}, shows that the magnitude of the residual flow increases with increasing slope of the bank, such that, the residual flow becomes more asymmetric around the crest of the asymmetric bank (Figure 8). In contrast, the asymmetry of the ratios V_{M_4}/V_{M_2}, V_{M_6}/V_{M_2} is only slightly modified in the asymmetric bank case when compared to that for symmetric ridges shown in Figure 8.

4. Diagnostic Analysis for Momentum Balance

[31] In order to understand how the bank morphology influences the Kelvin wave propagation, the tidal variability

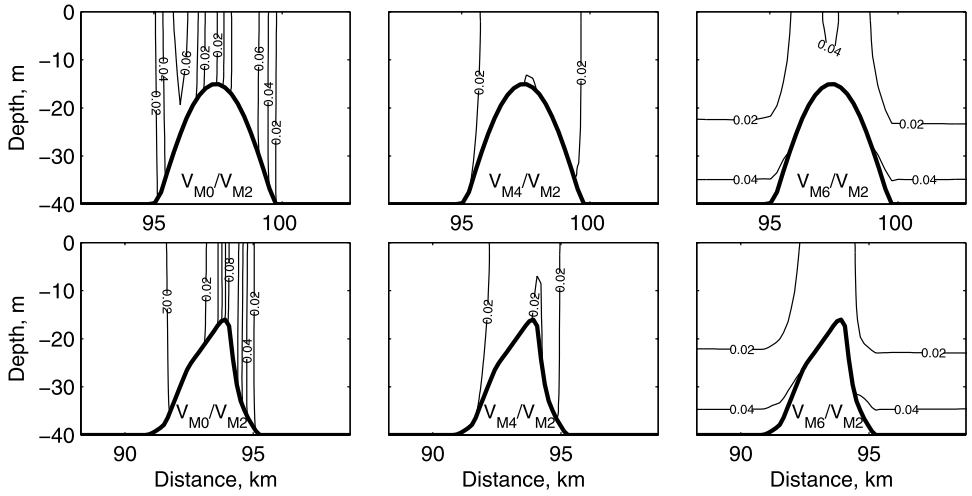

Figure 8. Cross-section plots of the speed ratio of mean flow (V_{M0}) and each overtide (V_{M4}, V_{M6}) to the semidiurnal tidal component speed V_{M2} for banks rotated 5° with (top) symmetric and (bottom) asymmetric bathymetric profiles, along transect BB′.

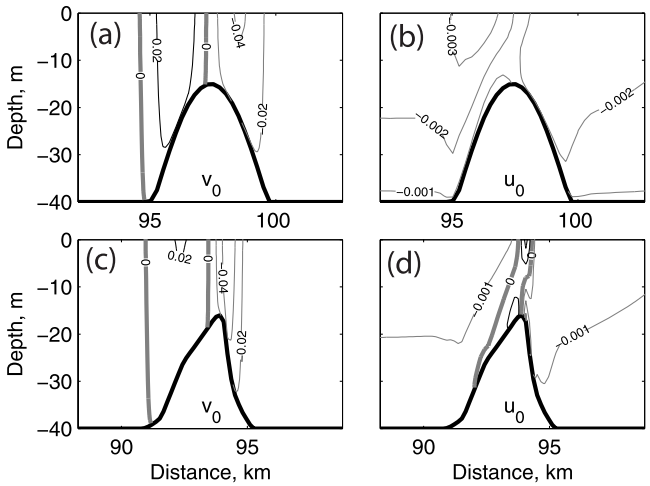

Figure 9. Cross-section plots of the along- and across-isobath residual flow (v_o' and u_o') for banks rotated 5° with (top) symmetric and (bottom) asymmetric bathymetric profiles, along transect BB′. Black contours represent positive values, while gray contours represent negative values. The thick gray contour represents the zero isotach.

of the terms of the momentum balance equation (see equations (7) and (8)) at 5 locations along the cross-shelf transect AA′ (see Figure 1) are shown in Figures 10 and 11 for levels near the sea surface and near the bed, respectively.

[32] The horizontal momentum balance equations used in this analysis are:

$$\frac{\partial u}{\partial t} = -u\frac{\partial u}{\partial x} - v\frac{\partial u}{\partial y} - w\frac{\partial u}{\partial z} + fv - \frac{1}{\rho}\frac{\partial p}{\partial x} + \frac{\partial}{\partial z}\left(k_v\frac{\partial u}{\partial z}\right) \quad (7)$$

$$\frac{\partial v}{\partial t} = -u\frac{\partial v}{\partial x} - v\frac{\partial v}{\partial y} - w\frac{\partial v}{\partial z} - fu - \frac{1}{\rho}\frac{\partial p}{\partial y} + \frac{\partial}{\partial z}\left(k_v\frac{\partial v}{\partial z}\right) \quad (8)$$

for the across- and along-shelf directions, respectively. The along-shelf tidal momentum balance in the flat areas (swales) is characterized by a progressive gravity wave, where the local acceleration ($\frac{\partial v}{\partial t}$) is mainly balanced by the pressure gradient ($-\frac{1}{\rho}\frac{\partial p}{\partial y}$) (Figure 10). At the slopes of the bank, horizontal advection ($-u\frac{\partial v}{\partial x} - v\frac{\partial v}{\partial y}$), vertical advection ($-w\frac{\partial v}{\partial z}$), vertical viscosity ($\frac{\partial}{\partial z}\left(k_v\frac{\partial v}{\partial z}\right)$) and Coriolis ($-fu$) force become also important. Both advection and vertical viscosity are equally important near the sea surface, while near the seabed advection is less important and vertical viscosity appears as the be the third term required to close the pressure-local acceleration balance. Over the crest, the magnitude of the advection term decreases while both vertical viscosity and Coriolis increase.

[33] Away from the bank area and on the swales, the across-shelf momentum balance is characterized by a quasi-geostrophic equilibrium (see Figure 11), as expected from the forcing (i.e., Kelvin wave) imposed at the northern open boundary. Over the banks that equilibrium is modified through the introduction of additional terms. In particular, near the bed, where the Coriolis force is reduced, the vertical viscosity term becomes important (see Figure 12, bottom row). At the slopes of the bank, the pressure gradient-Coriolis equilibrium is modified by the addition of the horizontal advection term at the surface and vertical viscosity near the bed. Over the crest, the quasi-geostrophic balance is modified by the increased values of the vertical viscosity term. The local acceleration term is relative small throughout the domain especially in the swales but increases with reduced water depth and attains its maximum value at the crest of the bank.

[34] Overall, away from the banks area and on the swales, the momentum balance describes a progressive Kelvin wave. Over the banks, advection and friction terms modify the across- and along-shelf momentum balance. Advective terms get their maximum values at the steepest parts of the bank, while frictional terms become important at the shallowest part and near the seabed. It is characteristic that maximum magnitudes of the along-bank M_4 and residual

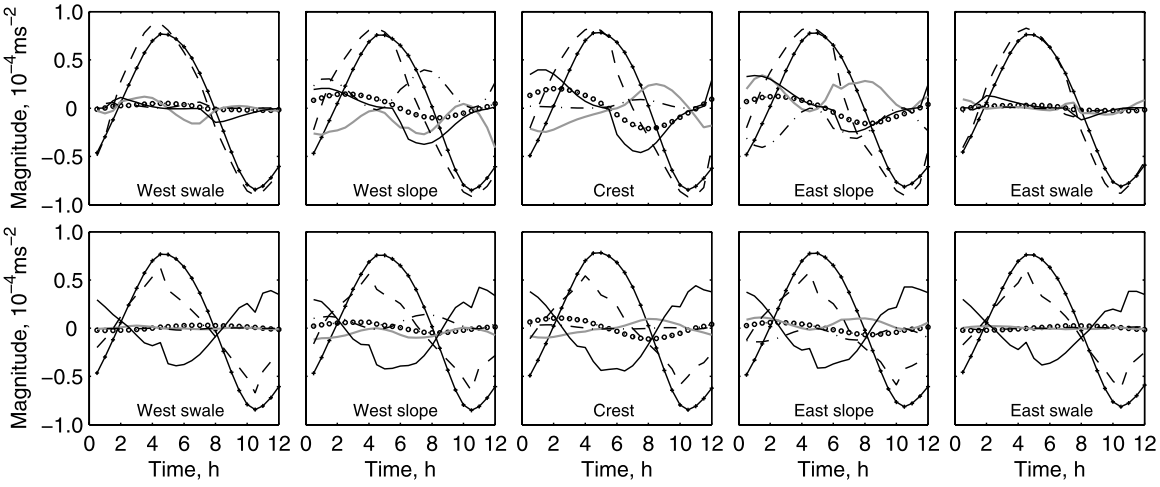

Figure 10. Significant terms of the along-shelf momentum balance equation at five different locations along the transect AA' and (top) at the surface and (bottom) near the corresponding to the baseline case. The lines legend is as follows: pressure gradient, black line with x marker; Coriolis force, black line with circles; horizontal advection, gray solid line; vertical advection, black dot-dashed line; vertical viscosity, black solid line; and local acceleration, black dashed line.

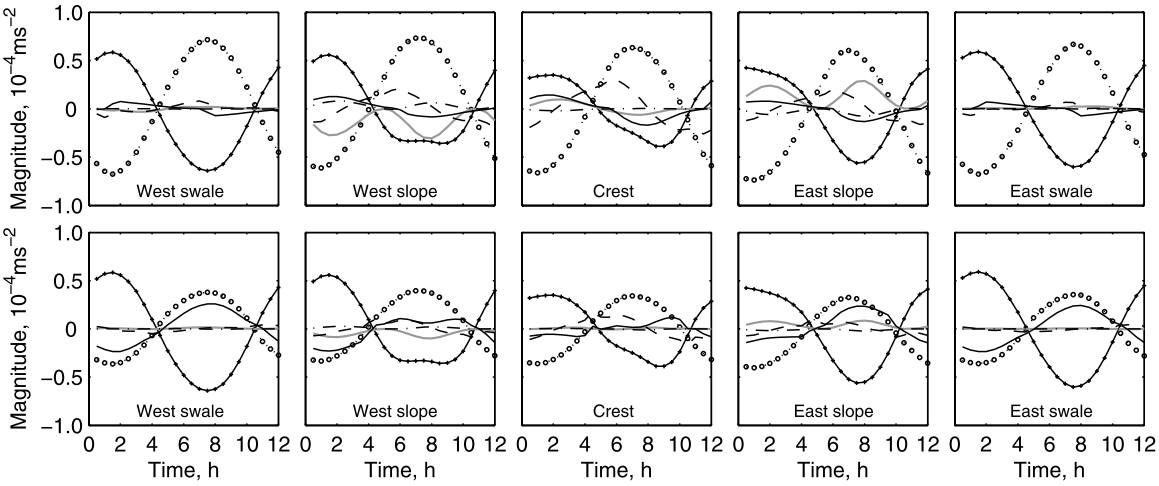

Figure 11. Significant terms of the across-shelf momentum balance equation at five different locations along the transect AA' and at two vertical levels: (top) surface and (bottom) near the bottom. The lines legend is as in Figure 10.

flow (see Figures 3 and 5) appear at the same location as the maximum values of advection (see Figures 10 and 11), while the distribution pattern of the magnitudes of the M_6 (see Figure 3c) is related with that of vertical viscosity terms (see Figures 10 and 11).

[35] Our numerical experiments show that the relative spatial variation of the individual major terms shown in equations (7) and (8) remain the same independently on bottom roughness and/or bank orientation. However, for the same location (e.g., swale and slope) the relative importance of the various terms varies depending on the case. This is shown in Figure 12, where time series of the horizontal momentum balance terms, near the bed at the western slope of the bank, are shown for cases 1 to 5. An increase on the bottom roughness (compare cases 1 and 2) leads to an increase of the vertical viscosity terms that corresponds to a reduction of the advection terms. In this case, the increased ratio V_{M4}/V_{M2} in case 2 as when compared to case 1 (see section 3) is solely due to friction. On the other hand, the relative importance of the advective and frictional terms increases when the angle between the principal tidal current and the bank axes increases (compare cases 3 and 5, Figure 12). In these cases the increment of the energy cascade toward higher harmonics and residual flow is due to both advection and friction.

5. Sediment Transport

[36] The net sediment transport proxy vector is estimated using equations (4) and (5) where u and v are the across- and along-shelf velocity components for the vertical level closest to the bottom, where sediment transport is most important.

5.1. Case 1 (Baseline)

[37] Net sediment fluxes describe a clockwise gyre similar to that observed on the residual flow, with the exception

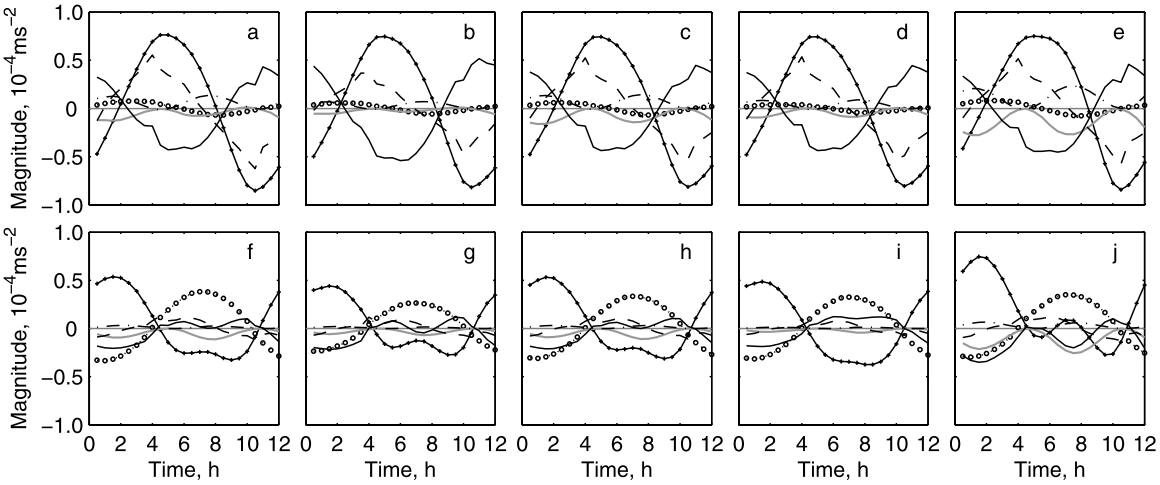

Figure 12. Significant terms of the (top) along- and (bottom) across-shelf momentum balance at the bottom part of the western slope corresponding to the numerical experiments with symmetric bank profile: (a) and (f) case 1; (b) and(g) case 2; (c) and (h) case 3; (d) and (i) case 4; and (e) and (j) case 5. The lines legend is as in Figure 10.

that the lateral (cross-bank) sediment flux converges toward the crest (Figure 13 (left)). The maximum magnitude of the proxy sediment flux is found at the slopes of the bank, while minimum values are obtained at the crest.

[38] The total sediment transport proxy vector S and that due to the residual ($\boldsymbol{S}_{res}$) and tidal asymmetries ($\boldsymbol{S}_{asym}$) are shown in Figure 13. The most important mechanism responsible for the net sediment transport is the residual flow (Figure 13 (middle)), while tidal asymmetries (Figure 13 (right)) appear to contribute less than 10% of the total (Figure 13 (left)). The most significant terms contributing to $\boldsymbol{S}_{res}$ are those that consist of the product of residual flow and the semidiurnal tidal component. Among the individual terms that constitute $\boldsymbol{S}_{asym}$ (see equations (4) and (5)), the most significant are those that are the product of the quarter-diurnal and semidiurnal tidal flows.

[39] Although the amplitude of the quarter-diurnal tidal flow component is larger on the eastern slope (see Figure 3), the main contribution of the tidal asymmetries to sediment transport is concentrated on the western slope (Figure 13 (right)). This is because of phase differences between the M_2 and M_4 that lead to a cosine factor ($cos(-\varphi_{4y} + 2\varphi_{2y})$) near zero on the eastern slope and almost 1 on the western side. As a result, the northward directed sediment transport due to the residual flow on the western slope is reduced by the southward directed sediment transport driven by the tidal asymmetries ($\boldsymbol{S}_{asym}$).

[40] According to the results presented in this section, the residual flow contributes the most to the total sediment transport. On the other hand, as mentioned in section 3, the cross-bank component of the residual flow (u') approaches to zero close to the seabed. Rewriting equations (4) and (5), so that the sediment transport proxy vector components are presented in the rotated reference frame (i.e., across- and along-bank directions) and ignoring the insignificant terms the across- and along-bank sediment transport proxies are:

$$\begin{aligned} S'_x = &\left\{ u'_2\left[v'_0 v'_2 \cos\left(\varphi_{2x} - \varphi_{2y}\right)\right] + u'_4\left[v'_0 v'_4 \cos\left(\varphi_{4x} - \varphi_{4y}\right)\right] + u'_6\left[v'_0 v'_6 \cos\left(\varphi_{6x} - \varphi_{6y}\right)\right]\right\} \qquad (I) \\ &\left\{ u'_4\left[\frac{3}{4}u'^2_2 \cos(-\varphi_{4x} + 2\varphi_{2x}) + \frac{1}{4}v'^2_2 \cos\left(\varphi_{4x} - 2\varphi_{2y}\right)\right]\right\} \qquad (II) \end{aligned} \tag{9}$$

and,

$$\begin{aligned} S'_y = &\left\{ v'_0\left[\left(v'^2_0 + u'^2_0\right) + \frac{1}{2}\left(3v'^2_2 + u'^2_2\right) + \frac{1}{2}\left(3v'^2_4 + u'^2_4\right) + \frac{1}{2}\left(3v'^2_6 + u'^2_6\right)\right]\right. \\ &\left. + v'_2\left[u'_2 u'_0 \cos\left(\varphi_{2x} - \varphi_{2y}\right)\right] + v'_4\left[u'_4 u'_0 \cos\left(\varphi_{4x} - \varphi_{4y}\right)\right] + v'_6\left[u'_6 u'_0 \cos\left(\varphi_{6x} - \varphi_{6y}\right)\right]\right\} \qquad (I) \\ &+ \left\{ v'_4\left[\frac{3}{4}v'^2_2 \cos\left(-\varphi_{4y} + 2\varphi_{2y}\right) + u'^2_2 \cos\left(\varphi_{4x} - 2\varphi_{2y}\right)\right]\right\} \qquad (II) \end{aligned} \tag{10}$$

In equations (9) and (10), the variables have been rearranged so that each term consists of the product of a sediment stirring (factor inside square brackets, units of $m^2\ s^{-2}$) and a sediment carrier parameter (factor outside square brackets, units of $m\ s^{-1}$).

[41] Such rearrangement facilitates the understanding of the cross-bank sediment transport mechanism and enables us to demonstrate that although the cross-bank residual flow is zero, the cross-bank sediment transport does not vanish. It is the interaction of the along-bank residual flow and tidal components of flow that set the sediment in motion (stirring, see term I in equation (9)) while the cross-shore tidal flows transport it. The net transport is controlled by the phase differences, as these are responsible for the maximum sediment motion (stirring) having a phase lag to the transporting tidal components. Term II in equation (9) shows cross-shore sediment transport also takes place in response to sediment mobilization by the semidiurnal tidal component and transported by the M_4 constituents. Term I in equation (9) contribute the most to the cross-bank sediment transport. Overall, these results indicate that it is the magnitude and the phase difference between the various tidal constituents that controls the cross-bank sediment transport, even when no cross-bank residual is present.

5.2. Relative Contribution of S_{res} and S_{asym} to the Net Sediment Transport Vector

[42] The relative contribution of $\boldsymbol{S}_{res}$ and $\boldsymbol{S}_{asym}$ to the net transport vector is assessed through the utilization of the dominance index (IDX) as defined in section 2 (equation (6)). Figure 14 (left) show the cross-bank (along BB′) variation of IDX for all numerical experiments. There it can be seen that IDX is positive everywhere over the bank except on the crest, which means, that $\boldsymbol{S}_{res}$ is larger than $\boldsymbol{S}_{asym}$ in most of the bank, except the locations (i.e., crest) where the residual flow is close to zero. This cross-bank variation of IDX is consistent along the whole bank.

[43] Comparing the net sediment flux from the different cases we identify common patterns: (1) a cyclonic gyre residual sediment transport, (2) convergence toward the crest, and (3) maximum sediment fluxes at the slopes of the bank. In the case of the symmetric cross-sectional bank profile cases, the parameter IDX (see Figure 14 (left)) reveals that (1) sediment flux due to residual flow is larger than that due to asymmetries in most of the bank area (e.g., dominance index positive); (2) tidal asymmetries contribute more to net sediment transport on the western slope than on the eastern slope (e.g., bigger dominance index on the eastern slope); and (3) sediment transport due to the residual flow and due to asymmetries becomes equally important over the crest of the bank (e.g., dominance index near zero). Although we have shown that overtides and residual flow increase as a result of the increased drag coefficient (from 3.5×10^{-3} to 7.5×10^{-3}), their increase is somehow proportional to each other, so that their contribution to net sediment transport does not change significant from the

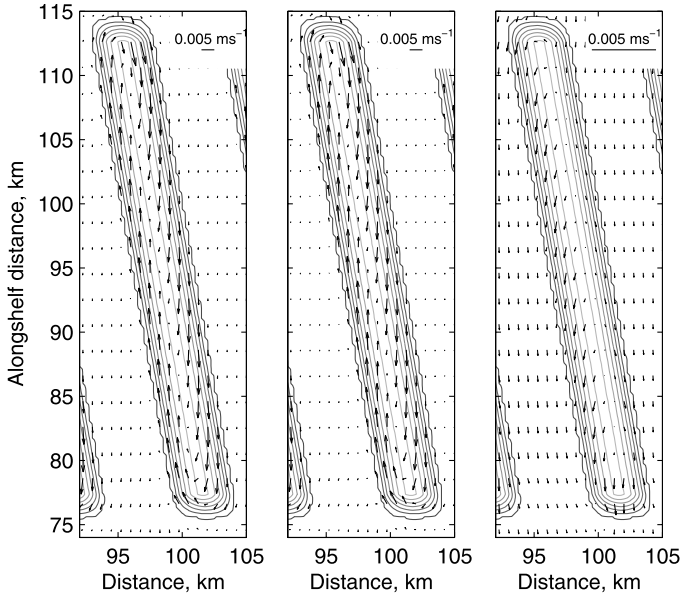

Figure 13. (left) Total sediment transport, (middle) net sediment transport flux due to the residual flow (S_{res}), and (right) net sediment fluxes due to tidal asymmetries (S_{asy}) for the vertical level closest to the bottom of the baseline case.

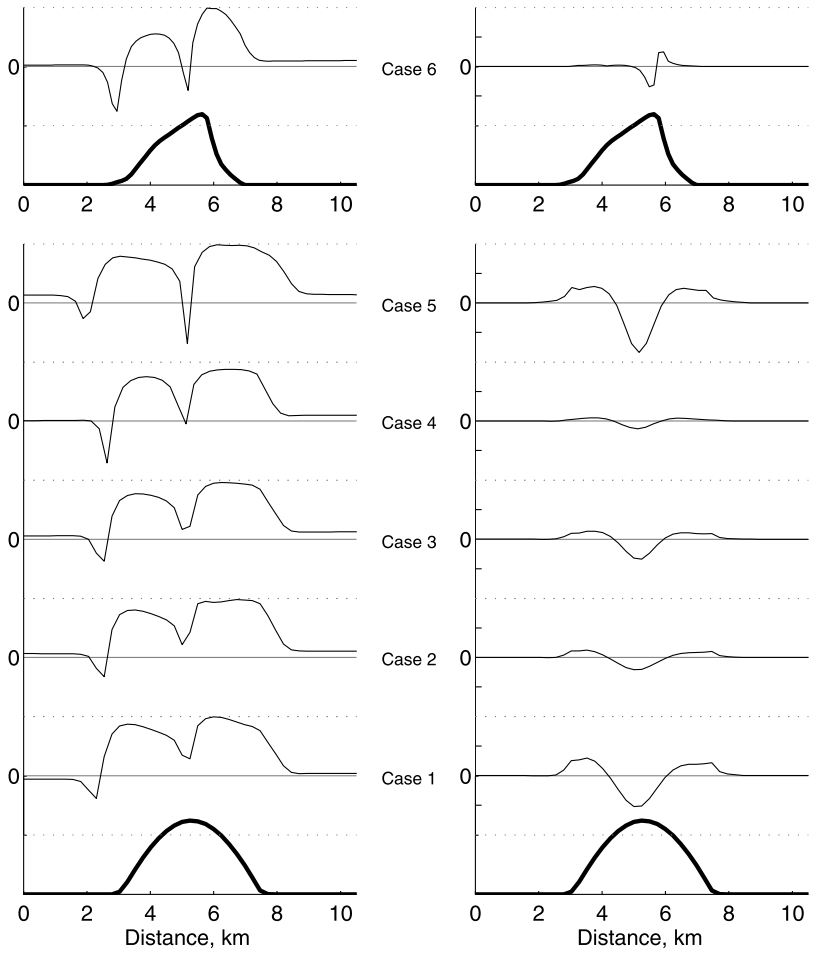

Figure 14. (left) Cross-isobath variation of IDX and (right) cross-isobath variation of net sediment fluxes divergence evaluated for the vertical level closest to the bottom, corresponding to all numerical experiments, along transect BB′. The horizontal dotted lines in the IDX plots represent one unit of IDX. The horizontal dotted lines in the divergence plots represent 4.0×10^{-6} m^3 s^{-3}/m.

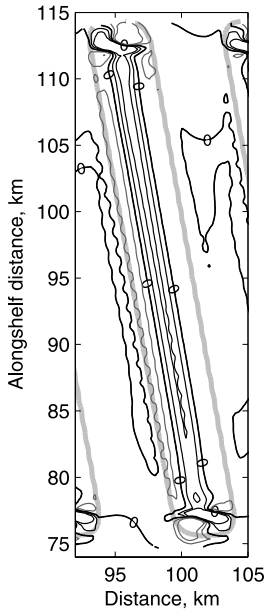

Figure 15. Contour plot of sediment divergence evaluated for the vertical level closest to the bottom for the baseline case. Black contours represent negative values, while gray contours represent positive values. Thick gray contour is the 39.9 m isobath, while the thick black contour represents the zero-divergence line. Units in 1×10^{-6} m^3 s^{-3}/m.

baseline case. On the other hand, an increase of the angle between the axis of the bank and the main tidal current results in an increase of energy cascade toward the higher harmonics and residual flow (see sections 3 and 4). However, the dominance index values (Figure 14) seem to be insensitive to changes of the angle of the bank. Thus, for a symmetric bank the relative importance of $\boldsymbol{S}_{asym}$ and $\boldsymbol{S}_{res}$ is the same and independent of both bottom roughness parameterization and bank orientation. Overall, net sediment transport is mainly driven by the residuals ($\boldsymbol{S}_{res}$), and according with the diagnostic analysis presented in section 4, advection is the biggest nonlinear term in the momentum balance that drives this process.

[44] For the case of an asymmetric bank, IDX is near 1 on the eastern, steeper slope, while on the western slope is only 0.5 (see Figure 14). So the contribution of the tidal asymmetries to sediment transport becomes noticeable on the gentle (western) slope. According to the features of the tidal and subtidal flow corresponding to the cases with a bank orientation of 5°(case 4 symmetric bank and case 6 asymmetric bank) shown in section 3, the ratio V_{m4}/V_{m2} remains similar for both cases, but the residual flow becomes strongly asymmetric with respect to the crest in the asymmetric bank case. This suggests that the low IDX values found on the western slope of the asymmetric bank correspond to the decreased residual flow rather than the increase of the tidal asymmetries (i.e., ratio V_{m4}/V_{m2}).

5.3. Sediment Divergence

[45] Sediment divergence is shown in Figure 15 as a contour diagram, where positive values indicate erosion and negative values indicate deposition. The 39.9 m isobath is also shown as a reference line. The zero divergence line is parallel to the isobaths but is located off the crest, between the crest and 39.9 m isobaths; it is located closer to the crest on the eastern side of the bank compared with the western side. This might suggest that an originally symmetric bank tends to be an asymmetric one.

[46] Figure 14 (right) show cross-bank variations of the net sediment transport proxy divergence corresponding to the vertical level closest to the bottom for all numerical experiments. All cases show a clear sediment convergence toward the crest and divergence on the slopes of the bank. Also all cases show maximum convergence location offset to the western slope.

[47] In the case where $Cd = 3.5 \times 10^{-3}$, sediment divergence is stronger on the western slope. An increased bottom drag or use of a spatially variable bottom drag leads to reduced divergences with similar magnitudes at both slopes of the bank. The minimum sediment divergence occurs for the case of a symmetric bank with a 5° orientation and increases as the bank orientation increases. So, in accordance to these results, more sediment erosional/acretional activity is expected on banks with low surface roughness or those that are more rotated with respect to the main tidal flow. The bank that is closed aligned to the tidal forcing shows the minimum erosional/depositional activity.

6. Conclusions

[48] Both residual flow and overtides are sensitive to bottom roughness parameterization and the orientation of the bank. For example, (1) the energy cascade toward the higher harmonics increases with increasing bottom roughness; (2) in the case of a spatially variable bottom roughness, the residual flow is reduced because of the roughness gradient mechanism that creates an anticlockwise vorticity (on anticlockwise rotated banks with bottom roughness pattern of rough-smooth-rough) that competes with the clockwise vorticity generated by the Coriolis and depth gradient mechanisms; (3) the magnitude of the principal overtide and the residual flow increases as the bank orientation increases; the former because of the increased of advection and the latter because of increased of differential velocity torque and torque due to gradient in depth distribution friction. It was found that the magnitude of the residual flow compared with the magnitude of the overtides was bigger independently of the bottom roughness parameterization and the value of "a".

[49] The analysis of the sediment transport proxies showed that cross-bank sediment transport can exist even if the cross-bank residual flow is zero. In such case, it is the magnitude and phase difference between the major tidal constituent and the overtides that control cross-bank sediment transport.

[50] In all numerical experiments, the net bed load sediment transport describes a gyre around the bank with clear convergence toward the crest. Although, the relative importance of $\boldsymbol{S}_{res}$ to $\boldsymbol{S}_{asym}$ is independent of the bank inclination or the bottom roughness parameterization, the "activity" (erosion/deposition) over the bank varies with bank inclination and the selected value of bottom roughness. For the cases of constant bottom roughness, the convergence/divergence of net sediment fluxes decreases

as roughness increases. So, although in a rough bank the sediment flux is larger, the erosion/deposition activity decreases. For the cases with spatially variable bottom roughness, the convergence/divergence of net sediment fluxes increases as the bank inclination (a) increases. So, according to our findings, the more active banks are those that are smooth (smaller roughness coefficients) or those more rotated respect to the main tidal current. The bank that is closed aligned to the tidal forcing shows the minimum convergence/divergence values. The zero divergence line is parallel to the isobaths, but is offset to the western slope, such that the sediment convergence/divergence distribution pattern suggests that the symmetric bank would have the tendency to become an asymmetric one.

[51] **Acknowledgments.** Funding for this work was provided by the U.S. Geological Survey as part of the SC Coastal Erosion Study and by the South Carolina Sea Grant Consortium (grant V169). Additional support for one of the authors (G. Voulgaris) was provided by the Office of Naval Research (Southeast Coastal Ocean Observing Systems) and by the National Science Foundation (award OCE-0451989).

References

Besio, G., P. Blondeaux, and G. Vittori (2006), On the formation of sand waves and sand banks, *J. Fluid Mech.*, *557*, 1–27.

Blondeaux, P. (2001), Mechanics of coastal forms, *Annu. Rev. Fluid Mech.*, *33*, 339.

Caston, V. N. D. (1972), Linear sandbanks in the southern North Sea, *Sedimentology*, *18*, 63–78.

Caston, V. N. D., and A. H. Stride (1970), Tidal sand movement between some linear sand banks in the southern North Sea, *Sedimentology*, *18*, 63–78.

Collins, M. B., S. J. Shimwell, S. Gao, H. Powell, C. Hewitson, and J. A. Taylor (1995), Water and sediment movement in the vicinity of linear sandbanks: The Norfolk Banks, southern North Sea, *Mar. Geol.*, *123*, 125–142.

Dronkers, J. J. (2005), *Dynamics of Coastal Systems,* 519 pp., World Sci., Hackensack, N. J.

Duane, D. B., M. E. Field, E. P. Meisburger, D. J. P. Swift, and S. J. Williams (1972), Linear shoals on the Atlantic inner continental shelf, Florida to Long Island, in *Shelf Sediment Transport: Process and Pattern*, edited by D. J. P. Swift, D. B. Duane, and O. H. Pilkey, pp. 447–498, Dowden, Hutchinson and Ross, Stroudsburg, Pa.

Dyer, K. R., and D. A. Huntley (1999), The origin, classification and modelling of sand bank and sand ridges, *Cont. Shelf Res.*, *19*, 1285–1330.

Griffiths, G., et al. (2002), Multidisciplinary ocean science applications of an AUV: The Autosub Science Missions Programme, in *Technology and Applications of Autonomous Underwater Vehicles,* edited by G. Griffiths, chap. 10, pp. 139–160, Taylor and Francis, London.

Gross, T. F., and F. E. Werner (1993), Residual circulation due to bottom roughness variability under tidal flow, *J. Phys. Oceanogr.*, *24*, 1494–1502.

Haidvogel, D. B., H. G. Arango, K. Hedstrom, A. Beckmann, P. Malanotte-Rizzoli, and A. F. Shchepetkin (2000), Model evaluation experiments in the North Atlantic basin: Simulations in nonlinear terrain-following coordinates, *Dyn. Atmos. Oceans.*, *32*, 239–281.

Hulscher, S. J. M. H., H. E. De Swart, and H. J. De Vriend (1993), The generation of offshore tidal sand banks and sand waves, *Cont. Shelf Res.*, *13*, 1183–1204.

Huthnance, J. M. (1973), Tidal current asymmetries over the Norfolk sandbanks, *Estuarine Coastal Mar. Sci.*, *1*, 89–99.

Huthnance, J. M. (1982a), On one mechanism forming linear sand banks, *Estuarine Coastal Shelf Sci.*, *14*, 74–99.

Huthnance, J. M. (1982b), On the formation of sand banks of finite extent, *Estuarine Coastal Shelf Sci.*, *15*, 277–299.

McCave, I. N. (1971), Sand waves in the North Sea off the coast of Holland, *Mar. Geol.*, *10*, 199–225.

McCave, I. N., and D. N. Langhorne (1982), Sand waves and sediment transport around the end of a tidal sand bank, *Sedimentology*, *29*, 95–110.

O'Connor, B. A. (Ed.) (1996), *Circulation and Sediment Transport Around Banks,* Univ. of Liverpool, Liverpool, U. K.

Parker, G., N. W. Lanfredi, and D. J. P. Swift (1982), Seafloor response to flow in a Southern Hemisphere sand ridge field: Argentine inner shelf, *Sediment. Geol.*, *33*, 195–216.

Pattiaratchi, C., and M. Collins (1987), Mechanisms for linear sand banks formation and maintenance in relation to dynamical oceanographic observations, *Prog. Oceanogr.*, *19*, 117–176.

Robinson, I. S. (1983), Tidally induced residual flows, in *Physical Oceanography of Coastal and Shelf Seas,* edited by B. Johns, pp. 321–356, Elsevier Sci., New York.

Roos, P. C., S. J. M. H. Hulscher, and M. A. F. Knaape (2004), The cross-sectional shape of tidal sandbanks: Modeling and observations, *J. Geophys. Res.*, *109*, F02003, doi:10.1029/2003JF000070.

Swift, D. J. P., and M. E. Field (1981), Evolution of a classic sand ridge field: Maryland sector, North American inner shelf, *Sedimentology*, *28*, 461–482.

Swift, D. J. P., G. Parker, M. W. Lanfredi, and G. Perillo (1978), Shoreface-connected sand ridges on American and European shelves: A comparison, *Estuarine Coastal Mar. Sci.*, *7*, 257–273.

Trowbridge, J. H. (1995), A mechanism for the formation and maintenance of shore-oblique sand ridges on storm-dominated shelves, *J. Geophys. Res.*, *100*, 16,071–16,086.

Umlauf, L., and H. Burchard (2003), A generic length-scale equation for geophysical turbulence models, *J. Mar. Res.*, *61*, 235–265.

Van der Molen, J. (2000), A 2DH numerical model of tidally induced sand transport in the North Sea, in *Interactions Between Estuaries, Coastal Seas and Shelf Seas,* edited by T. Yanagi, pp. 265–285, Terra Sci., Tokyo.

Vanwesenbeeck, V., and J. Lanckneus (2000), Residual sediment transport paths on a tidal sand bank: A comparison between the modified McLaren model and bedform analysis, *J. Sedimentary Res.*, *70*, 470–477.

Voulgaris, G., J. H. Trowbridge, and E. Terray (2001), Spatial variability of bottom turbulence over a linear sand ridge: Mooring deployment and AUTOSUB AUV survey cruise report, *Tech. Rep. WHOI-2001–09,* 41 pp., Woods Hole Oceanogr. Inst., Woods Hole, Mass.

Voulgaris, G., J. H. Trowbridge, and E. Terray (2002), AUV-based flow and turbulence gradient measurements: The wish of a modeler, *Eos Trans. AGU*, *83*(4), Ocean Sci. Meet. Suppl., Abstract OS22K-10.

Warner, J. C., C. R. Sherwood, H. G. Arango, and R. P. Signell (2005), Performance of four turbulence closure models implemented using a generic length scale method, *Ocean Modell.*, *8*, 81–113.

Williams, J. J., N. J. MacDonald, B. A. O'Connor, and S. Pan (2000), Offshore sand bank dynamics, *J. Mar. Syst.*, *24*, 153–173.

Zimmerman, J. T. F. (1980), Vorticity transfer by tidal currents over an irregular topography, *J. Mar. Res.*, *38*, 601–630.

R. Sanay and G. Voulgaris, Marine Science Program, Department of Geological Sciences, University of South Carolina, 701 Sumter Street, EWS617, Columbia, SC 29208, USA. (rsanay@geol.sc.edu; gvoulgaris@geol.sc.edu)

J. C. Warner, Coastal and Marine Geology Program, U.S. Geological Survey, 384 Woods Hole Road, Woods Hole, MA 02543, USA. (jcwarner@usqs.gov)